

A Directional Borehole Radar System *

Koen W.A. van Dongen^{a)}, Ronald van Waard^{a)}, Stefan van der Baan^{a)},
Peter M. van den Berg^{b)} and Jacob T. Fokkema^{b)}

^{a)} T&A RADAR,

Badhuisweg 3, PO Box 37060, 1030 AB Amsterdam, The Netherlands

^{b)} Centre for Technical Geoscience, Delft University of Technology,
PO Box 5031, 2600 GA Delft, The Netherlands

30th January 2002

1 Introduction

There are many situations all over the world where one would like to know how the subsurface is built up. Electromagnetic measurements with ground penetrating radar (GPR) from the surface might give an answer, but problems arise if the volume of interest is unreachable for such methods. For example in the oil and gas industry where the oil containing sand layer of interest, especially the top and the bottom of an oil reservoir, is simply too deep. In such case GPR measurements in a borehole is then a good solution as long as the system is directional. Unfortunately, with these systems directionality is often offset against penetration. The radar system we present fits in a single borehole. In addition it combines directionality and large penetration by focusing the emitted energy. The system has in both radial and angular direction a good resolution. First we discuss the modeling and design of the antenna system which consists of an electric dipole and a curved reflector. The radiation pattern of the antenna system is computed by first solving the integral equation for the unknown electric surface current density on the reflector. This is done via a FFT Conjugate Gradient method. Next the total electric wavefield is computed using the integral representation over the dipole and the reflector. Finally we discuss an imaging method to obtain a three-dimensional image of the subsurface. Here a one step deconvolution of the measured data for the computed radiation pattern is carried out. Imaging results based on both synthetic data and measured data will be shown.

2 Antenna Design

The antenna system contains an electric dipole which is partly shielded by a curved reflector. In order to compute the effect of the reflector on the omni-directional radiation pattern of the electric dipole antenna, an integral equation is derived. This equation relates the known incident electric wavefield from the electric dipole antenna with the unknown electric surface current density at the reflector. Once the discretised integral

*article for: *International Symposium on the State of Art of GPR, TNO Physics and Electronics Laboratory, The Hague, The Netherlands, June 8, 2001.*

equation is solved, via a FFT Conjugate Gradient method, the electric wavefield from the dipole shielded with the total reflector is computed. A numerical example will show the focusing effect of the reflector and some experimental results are used to verify our numerical results.

2.1 Antenna configuration

A position in the Cartesian coordinate system is denoted by the vector $\mathbf{x} = x_i = (x, y, z)$ whereas the same position is described in the orthogonal circular cylindrical coordinate system by the vector $\mathbf{v} = v_i = \{x, r, \phi\}$. The correspondence between both vectors is given by

$$\{x, y, z\} = \{x, r \cos(\phi), r \sin(\phi)\} , \quad (1)$$

see figure 1. Consequently the coordinate transformation matrices \mathbf{T}_{ij} and \mathbf{T}_{ij}^{-1} are defined via

$$u_{x_i}(\mathbf{v}) = \mathbf{T}_{ij} u_{v_j}(\mathbf{v}) , \quad u_{v_i}(\mathbf{v}) = \mathbf{T}_{ij}^{-1} u_{x_j}(\mathbf{v}) , \quad (2)$$

where $u_{x_i}(\mathbf{v})$ and $u_{v_i}(\mathbf{v})$ are both positioned in the cylindrical coordinate system at \mathbf{v} , defined in the Cartesian and cylindrical coordinate system and pointing in the direction x_i and v_i respectively. Note that we use Einstein's summation convention for repeated subscripts.

The dipole is defined in the cylindrical coordinate system in the spatial domain \mathbb{D} ,

$$\mathbb{D} = \{v_i \in \mathbb{R}^3 \mid -d_1 < x < d_1, r = d_2, \phi = d_3\} . \quad (3)$$

Next to the dipole, a perfectly conducting rectangular circular cylindrical curved plate acts as a reflector. The area \mathbb{A} of this reflector is defined in the cylindrical coordinate system as

$$\mathbb{A} = \{v_i \in \mathbb{R}^3 \mid -a_1 < x < a_1, r = a_2, -a_3 < \phi < a_3\} . \quad (4)$$

The configuration is embedded in a homogeneous medium with constant electric permittivity ε , vacuum magnetic permeability μ_0 and electric conductivity σ . Here permittivity ε equals

$$\varepsilon = \varepsilon_0 \varepsilon_r , \quad (5)$$

where ε_0 equals the permittivity of vacuum and ε_r the relative permittivity of the medium.

Our analysis is carried out in the temporal Laplace domain, with Laplace parameter $s = -i\omega$, where ω equals $2\pi f$ with f the frequency. Throughout this chapter we use the symbol $\hat{\cdot}$ to indicate that the specified quantity is in this temporal Laplace domain.

2.2 Formulation of the integral equation

The electric part of the wavefield generated by the dipole, in absence of the reflector, is denoted as $\hat{E}_{x_i}^{\text{dip}}(\mathbf{x})$. The total field in presence of the reflector is given by $\hat{E}_{x_i}^{\text{tot}}(\mathbf{x})$. Then, the scattered field due to the presence of the reflector, is defined as $\hat{E}_{x_i}^{\text{sct}}(\mathbf{x})$,

$$\hat{E}_{x_i}^{\text{sct}}(\mathbf{x}) = \hat{E}_{x_i}^{\text{tot}}(\mathbf{x}) - \hat{E}_{x_i}^{\text{dip}}(\mathbf{x}) , \quad \forall \mathbf{x} \in \mathbb{R}^3 . \quad (6)$$

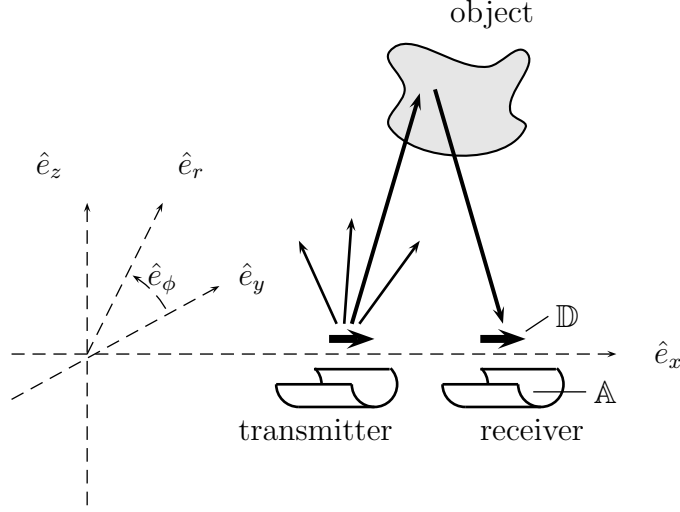


Figure 1: The bistatic antenna configuration and the two coordinate systems: the Cartesian with unit vectors $\{\hat{\mathbf{e}}_x, \hat{\mathbf{e}}_y, \hat{\mathbf{e}}_z\}$ and the cylindrical with unit vectors $\{\hat{\mathbf{e}}_x, \hat{\mathbf{e}}_r, \hat{\mathbf{e}}_\phi\}$.

The wavefield from an electric dipole in a Cartesian coordinate system can be derived from Maxwell equations and equals

$$\begin{aligned} \hat{E}_{x_i}^{\text{dip}}(\mathbf{x}) &= \frac{1}{s\varepsilon} \left(-\hat{\gamma}^2 \delta_{ij} + \nabla_{x_i} \nabla_{x_j} \cdot \right) \int_{\mathbf{x}' \in \mathbb{D}} \hat{G}(\mathbf{x}|\mathbf{x}') \hat{J}_{x_j}^{\text{dip}}(\mathbf{x}') dA(\mathbf{x}') \\ &= \frac{1}{s\varepsilon} \left(-\hat{\gamma}^2 \delta_{ij} + \nabla_{x_i} \nabla_{x_j} \cdot \right) \hat{A}_{x_j}^{\text{dip}}(\mathbf{x}) , \end{aligned} \quad (7)$$

with

$$\hat{\gamma}^2 = s^2 \left(\varepsilon + \frac{\sigma}{s} \right) \mu_0 , \quad (8)$$

δ_{ij} the Kronecker delta tensor, $\nabla_{x_i} \nabla_{x_j} \cdot$ the gradient divergence operator, $\hat{G}(\mathbf{x}|\mathbf{x}')$ the Green's function of the medium, $\hat{A}_{x_j}^{\text{dip}}(\mathbf{x})$ the electric vector potential and where $\hat{J}_{x_j}^{\text{dip}}(\mathbf{x}')$ is obtained from a unit time domain delta pulse electric surface current density at the dipole. Using the coordinate transformation matrices defined in equation (2), equation (7) is formulated in a cylindrical coordinate system as

$$\hat{E}_{v_i}^{\text{dip}}(\mathbf{v}) = \frac{1}{s\varepsilon} \left(-\hat{\gamma}^2 \delta_{ij} + \nabla_{v_i} \nabla_{v_j} \cdot \right) \hat{A}_{v_j}^{\text{dip}}(\mathbf{v}) , \quad (9)$$

with

$$\hat{A}_{v_j}^{\text{dip}}(\mathbf{v}) = \mathsf{T}_{jk} \int_{\mathbf{v}' \in \mathbb{D}} \hat{G}(\mathbf{v}|\mathbf{v}') \mathsf{T}_{kl}^{-1} \hat{J}_{v_l}^{\text{dip}}(\mathbf{v}') dA(\mathbf{v}') . \quad (10)$$

The scattered wavefield is caused by an electric surface current density at the surface of the reflector, due to the presence of the incident electric wavefield, and is given by

$$\hat{E}_{v_i}^{\text{sct}}(\mathbf{v}) = \frac{1}{s\varepsilon} \left(-\hat{\gamma}^2 \delta_{\alpha j} + \nabla_{v_i} \nabla_{v_j} \cdot \right) \hat{A}_{v_j}^{\text{sct}}(\mathbf{v}) , \quad (11)$$

with

$$\hat{A}_{v_j}^{\text{sct}}(\mathbf{v}) = \mathsf{T}_{jk} \int_{\mathbf{v}' \in \mathbb{A}} \hat{G}(\mathbf{v}|\mathbf{v}') \mathsf{T}_{kl}^{-1} \hat{J}_{v_l}^{\text{rfl}}(\mathbf{v}') d\mathbf{A}(\mathbf{v}') , \quad (12)$$

where $\hat{J}_{v_m}^{\text{rfl}}(\mathbf{v}') = \left\{ \hat{J}_x^{\text{rfl}}(\mathbf{v}'), 0, \hat{J}_\phi^{\text{rfl}}(\mathbf{v}') \right\}$ are the two unknown surface current densities at the reflector. At this surface, electromagnetic boundary conditions require that components of the total electric field, $\hat{E}_{v_i}^{\text{tot}}(\mathbf{v})$, tangential to this surface vanish and therefore

$$\hat{E}_{v_\alpha}^{\text{sct}}(\mathbf{v}) = -\hat{E}_{v_\alpha}^{\text{dip}}(\mathbf{v}) , \quad \forall \mathbf{v} \in \mathbb{A} , \quad \forall \alpha \in \{1, 3\} , \quad (13)$$

where we use Greek subscripts α and β to denote the tangential character of the quantity. Taking the point of observation on the reflector, we end up with following integral equation

$$-\hat{E}_{v_\alpha}^{\text{dip}}(\mathbf{v}) = \frac{1}{s\varepsilon} \left(-\hat{\gamma}^2 \delta_{\alpha j} + \nabla_{v_\alpha} \nabla_{v_j} \cdot \right) \hat{A}_{v_j}^{\text{sct}}(\mathbf{v}) , \quad (14)$$

where the vector potential $\hat{A}_{v_j}^{\text{sct}}(\mathbf{v})$ is defined in (12).

2.3 Solution of the integral equation

Combining equations (14) and (12) we write the integral equation as

$$-\hat{E}_{v_\alpha}^{\text{dip}}(\mathbf{v}) = \frac{1}{s\varepsilon} \left(-\hat{\gamma}^2 \delta_{\alpha j} + \nabla_{v_\alpha} \nabla_{v_j} \cdot \right) \mathsf{T}_{jk} \int_{\mathbf{v}' \in \mathbb{A}} \hat{G}(\mathbf{v}|\mathbf{v}') \tilde{\mathsf{T}}_{k\beta}^{-1} \hat{J}_{v_\beta}^{\text{rfl}}(\mathbf{v}') d\mathbf{A}(\mathbf{v}') , \quad (15)$$

in which we have defined the following known and unknown quantities:

$$\hat{J}_{v_\beta}^{\text{rfl}}(\mathbf{v}) = \begin{pmatrix} \hat{J}_x^{\text{rfl}}(\mathbf{v}) \\ \hat{J}_\phi^{\text{rfl}}(\mathbf{v}) \end{pmatrix} , \quad \hat{E}_{v_\alpha}^{\text{dip}}(\mathbf{v}) = \begin{pmatrix} \hat{E}_x^{\text{dip}}(\mathbf{v}) \\ \hat{E}_\phi^{\text{dip}}(\mathbf{v}) \end{pmatrix} , \quad (16)$$

the matrices

$$\tilde{\mathsf{T}}_{k\beta}^{-1} = \begin{pmatrix} 1 & 0 \\ 0 & -\sin(\phi) \\ 0 & \cos(\phi) \end{pmatrix} , \quad \mathsf{T}_{jk} = \begin{pmatrix} 1 & 0 & 0 \\ 0 & \cos(\phi) & \sin(\phi) \\ 0 & -\sin(\phi) & \cos(\phi) \end{pmatrix} , \quad \delta_{\alpha j} = \begin{pmatrix} 1 & 0 & 0 \\ 0 & 0 & 1 \end{pmatrix} , \quad (17)$$

and the gradient divergence operator

$$\nabla_{v_\alpha} \nabla_{v_j} \cdot = \begin{pmatrix} \partial_x^2 & \frac{1}{r} \partial_x \partial_r r & \frac{1}{r} \partial_x \partial_\phi \\ \frac{1}{r} \partial_\phi \partial_x & \frac{1}{r^2} \partial_\phi \partial_r r & \frac{1}{r^2} \partial_\phi^2 \end{pmatrix} . \quad (18)$$

Note that the $\tilde{\mathsf{T}}_{k\beta}^{-1}$ is obtained from T^{-1} , the inverse of T . Equation (15) is solved numerically using a discretisation procedure as suggested by Zwamborn and van den Berg [1]. Therefore we approximate the differential operator of equation (18) by a finite difference operator [2]. Furthermore the plate domain is discretised into subdomains \mathbb{A}_{mn} as shown in figure 2, viz.

$$\mathbb{A}_{mn} = \{ \mathbf{v} \in \mathbb{R}^3 | x_{m-1} < x < x_m, r = a_2, \phi_{n-1} < \phi < \phi_n \} , \quad (19)$$

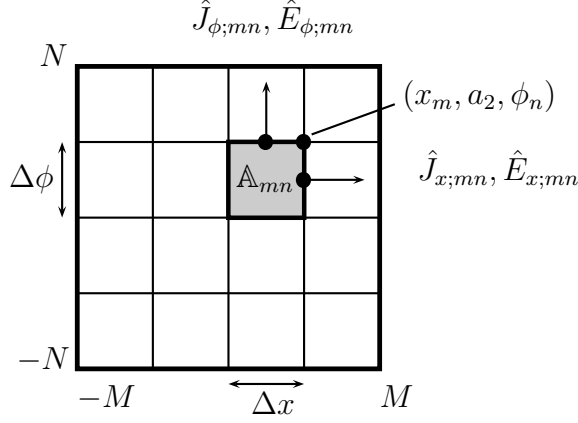


Figure 2: The discretisation of the plate domain \mathbb{A} into subdomains \mathbb{A}_{mn} .

for

$$x_m = m\Delta x, \quad \text{for } m = -M, \dots, M, \quad (20)$$

$$\phi_n = n\Delta\phi, \quad \text{for } n = -N, \dots, N. \quad (21)$$

The quantities $\hat{E}_{v_\alpha}^{\text{dip}}(\mathbf{v})$ and $\hat{J}_{v_\alpha}^{\text{rf}}(\mathbf{v})$ are defined on a staggered grid as shown in figure 2,

$$\hat{E}_{v_\alpha}^{\text{dip}}(\mathbf{v}) = \begin{pmatrix} \hat{E}_{x_{mn}}^{\text{dip}} \\ \hat{E}_{\phi_{mn}}^{\text{dip}} \end{pmatrix} = \begin{pmatrix} \hat{E}_x^{\text{dip}}(m\Delta x, a_2, (n - \frac{1}{2})\Delta\phi) \\ \hat{E}_\phi^{\text{dip}}((m - \frac{1}{2})\Delta x, a_2, n\Delta\phi) \end{pmatrix}, \quad (22)$$

for $m = -M, \dots, M$ and $n = -N, \dots, N$,

$$\hat{J}_{v_\beta}^{\text{rf}}(\mathbf{v}) = \begin{pmatrix} \hat{J}_{x_{mn}}^{\text{rf}} \\ \hat{J}_{\phi_{mn}}^{\text{rf}} \end{pmatrix} = \begin{pmatrix} \hat{J}_x^{\text{rf}}(m\Delta x, a_2, (n - \frac{1}{2})\Delta\phi) \\ \hat{J}_\phi^{\text{rf}}((m - \frac{1}{2})\Delta x, a_2, n\Delta\phi) \end{pmatrix}, \quad (23)$$

for $m = -M, \dots, M$ and $n = -N, \dots, N$.

The consequently obtained discretised integral equation is solved using a FFT Conjugate Gradient method as in [1]. Therefore we replace our integral equation by an operator equation, viz.

$$\mathbf{f}_{v_\alpha} = (\mathbf{Lj})_{v_\alpha}, \quad (24)$$

where \mathbf{f}_{v_α} is obtained from the known incident wavefield, and $(\mathbf{Lj})_{v_\alpha}$ the operation \mathbf{L} applied on the electric surface current density \mathbf{j} on the reflector. Furthermore, we define the L_2 norm via the inner product of two vectorial quantities in the spatial domain \mathbb{A} , viz.

$$\begin{aligned} \|u_{v_\alpha}\|_{\mathbb{A}}^2 &= \langle u_{v_\alpha}, \bar{u}_{v_\alpha} \rangle_{\mathbb{A}} \\ &= \sum_{m=-M+1}^{M-1} \sum_{n=-N+1}^N u_{x;mn} \bar{u}_{x;mn} a_2 \Delta x \Delta\phi + \sum_{m=-M+1}^M \sum_{n=-N+1}^{N-1} u_{\phi;mn} \bar{u}_{\phi;mn} a_2 \Delta x \Delta\phi, \end{aligned} \quad (25)$$

in which the overbar denotes the complex conjugate. To quantify the residual $\mathbf{f}_{v_\alpha} - (\mathbf{Lj})_{v_\alpha}$ for equation (24) we define the error norm

$$r_{v_\alpha} = \|\mathbf{f}_{v_\alpha} - (\mathbf{Lj})_{v_\alpha}\|_{\mathbb{A}}. \quad (26)$$

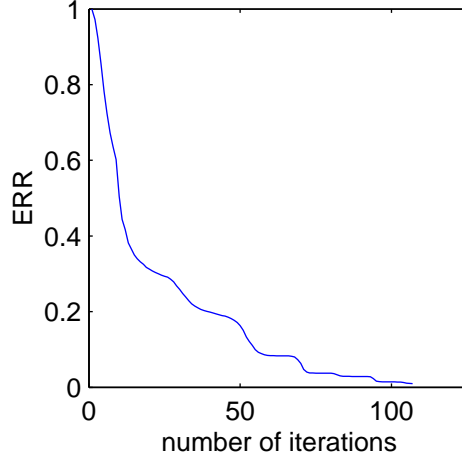


Figure 3: The normalized error ERR as a function of the number of iterations.

Finally, the normalized error function ERR which is minimized is defined as

$$ERR = \frac{\|r_{v_\alpha}\|_{\mathbb{A}}}{\|\hat{E}_{v_\alpha}^{\text{dip}}\|_{\mathbb{A}}} . \quad (27)$$

2.4 Numerical and experimental results

Simulations are carried out to design an optimal configuration. The dipole is positioned at a radial distance of approximately 0.05 m. The reflector is positioned at the same radial distance and curved over approximately 150° and we use 26 cells in the x -direction and 16 cells in the ϕ -direction. The system is embedded in a non-conducting medium, $\sigma = 0$, with relative permittivity $\varepsilon_r = 80$. Computations are carried out for the 100 MHz components of the electromagnetic wavefields and the iterative process is stopped when the normalized error satisfies $ERR \leq 0.01$. In figure 3 we present the normalized error as a function of the number of iterations. The results for the electric surface current densities are shown in figure 4. From this figure we observe that the components of the current densities normal to the edges vanish, as we expect. But the components tangential to the edges tend to large values, in fact theoretically they should grow to infinity.

Using these surface currents we compute the scattered and total electric wavefields. In figures 5(a) and 5(b) the total electric wavefield in the plane $x = 0$ and $y = 0$ are shown. Clearly visible is the effect of the presence of the reflector on the radiation pattern of a dipole. However, the aim is not only to disturb the omni-directional radiation pattern of an electric dipole but also to increase penetration into the subsurface by focusing the wavefield. Therefore it is interesting to compute the gain factor $|E^{\text{tot}}|/|E^{\text{dip}}|$, as shown in figures 6(a) and 6(b).

Based on this design a prototype antenna system is built for experimental verification of the antenna model. The radiation pattern of this prototype is measured at a radial distance of $r = 0.3$ m in the plane $x = 0$. In figure 7 the measured and computed radiation patterns are shown. Both curves are normalized by putting their maximum values to unity. We observe an excellent agreement between both curves.

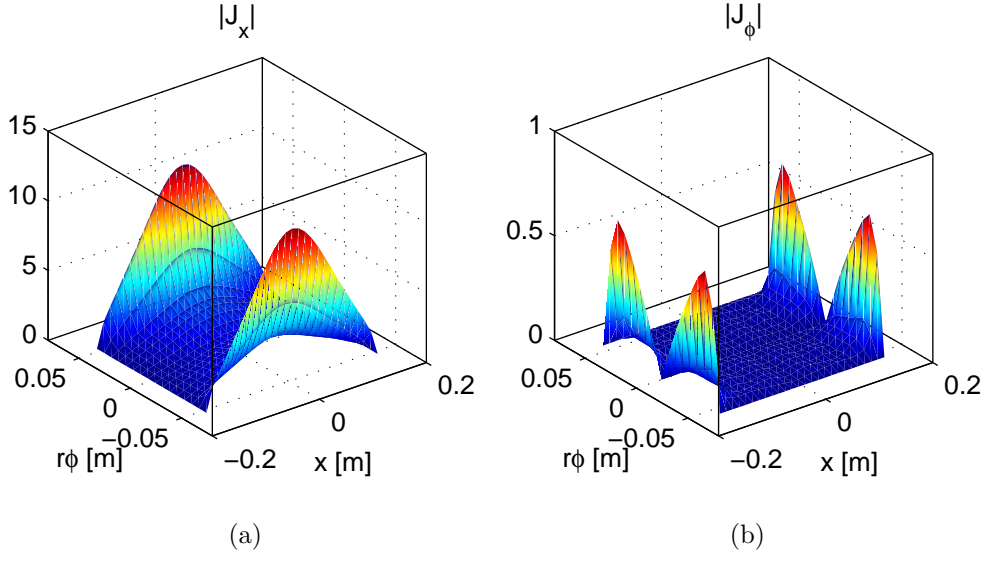


Figure 4: The electric surface current density at the surface of the reflector: (a) the absolute value of J_x and (b) the absolute value of J_ϕ .

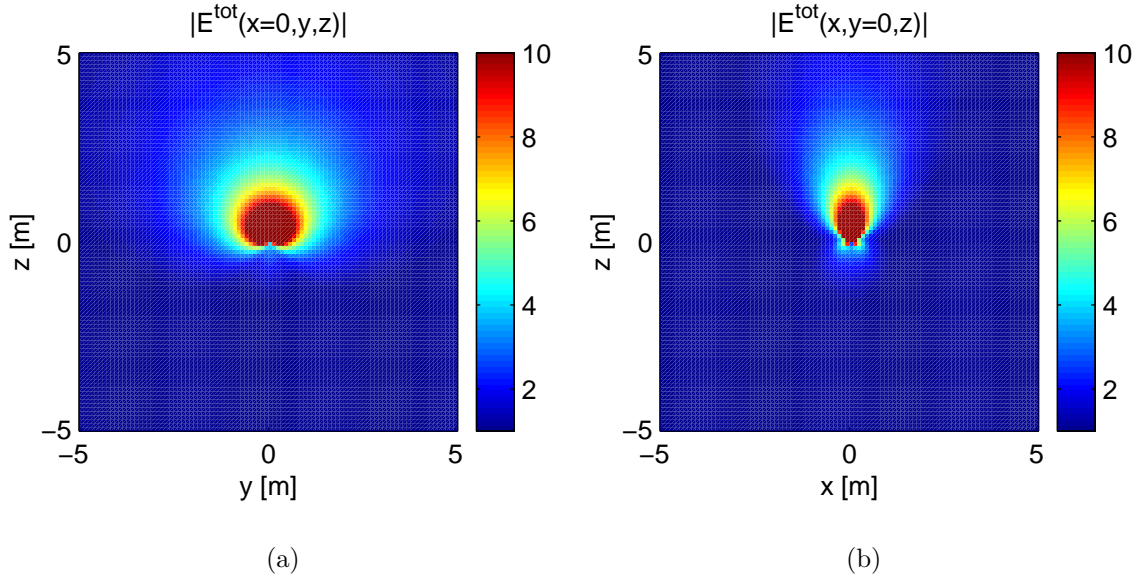


Figure 5: The computed total electric wavefield in the plane (a) $x = 0$ and (b) $y = 0$.

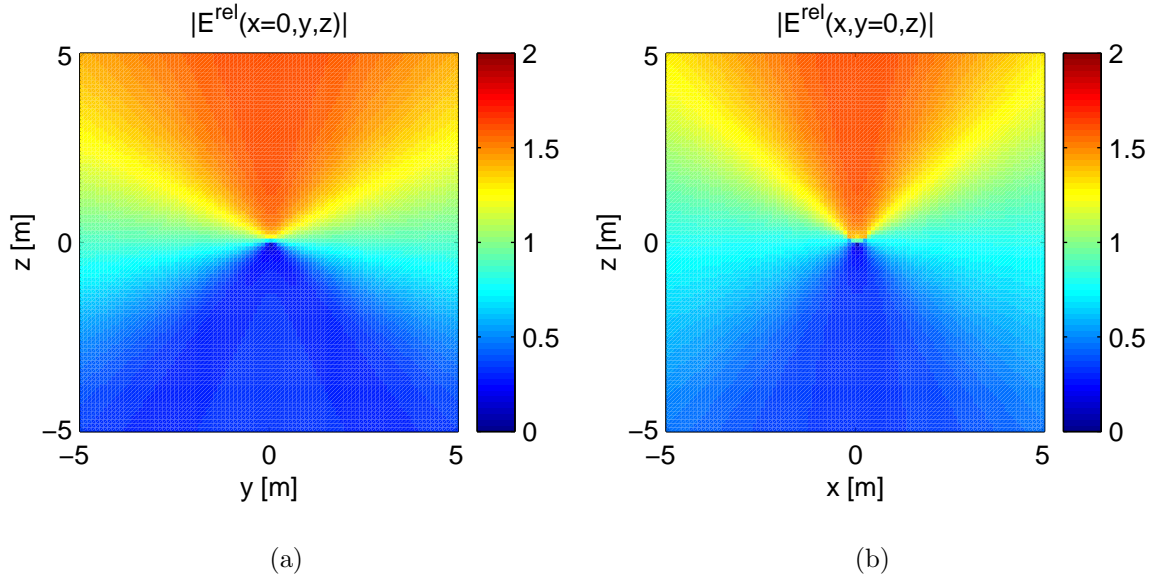


Figure 6: The normalized electric wavefield, $|E^{\text{rel}}(\mathbf{x})| = \frac{|E^{\text{tot}}(\mathbf{x})|}{|E^{\text{dip}}(\mathbf{x})|}$, in the plane (a) $x = 0$ and (b) $y = 0$.

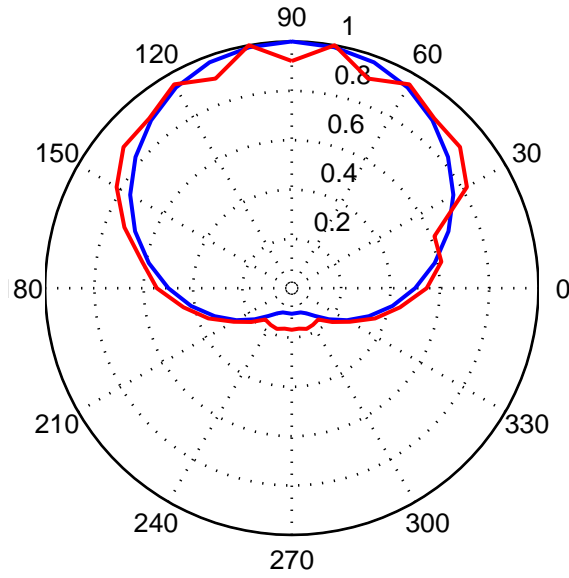


Figure 7: The computed (solid line) and measured (crosses) normalized radiation pattern.

Table 1: Description of the states A and B for the spatial domain \mathbb{D}

state A	state B
$\{\hat{E}_p^A, \hat{H}_q^A\} = \{\hat{E}_p^{\text{bg}}, \hat{H}_q^{\text{bg}}\}$	$\{\hat{E}_p^B, \hat{H}_q^B\} = \{\hat{E}_p^{\text{tot}}, \hat{H}_q^{\text{tot}}\} = \{\hat{E}_p^{\text{bg}} + \hat{E}_p^{\text{sct}}, \hat{H}_q^{\text{bg}} + \hat{H}_q^{\text{sct}}\}$
$\{\hat{\eta}^A, \hat{\zeta}^A\} = \{\hat{\eta}^{\text{bg}}, \hat{\zeta}\}$	$\{\hat{\eta}^B, \hat{\zeta}^B\} = \left\{ \left(\hat{\eta}^{\text{sct}}, \hat{\zeta} \right), \left(\hat{\eta}^{\text{bg}}, \hat{\zeta} \right) \right\} \{ \mathbf{x} \in \mathbb{D}^{\text{sct}}, \mathbf{x} \notin \mathbb{D}^{\text{sct}} \}$
$\{\hat{J}_p^A, \hat{K}_q^A\} = \{0, 0\}$	$\{\hat{J}_p^B, \hat{K}_q^B\} = \{0, 0\}$

3 Imaging Based on Back Propagation

The imaging algorithm described in this section is based on a deconvolution of the measured data for the previously computed radiation pattern of the antenna system. Starting with the reciprocity theorem an integral equation is derived which describes the change of impedance of the antenna system as a function of the change in contrast in the background medium. An approximate solution of this integral equation, and consequently a 3D image of the subsurface, is obtained via a one step inversion procedure, the so called back propagation.

3.1 Change of antenna impedance due to anomalies in the background medium

The reciprocity theorem [3] is used to correlate two field states occurring in the same spatial domain \mathbb{D} . In figure 8, the two states A and B are shown as described in table 1. In state A, the closed surface $\partial\mathbb{D}$ with normal ν_i encloses the source free spatial domain \mathbb{D} which is a homogeneous background medium that is, in addition, linear, time-invariant, instantaneously reacting, locally reacting and isotropic in its electromagnetic behaviour. The medium is described by the parameters $\hat{\eta}^{\text{bg}}(\mathbf{x})$,

$$\hat{\eta}^{\text{bg}}(\mathbf{x}) = \sigma^{\text{bg}}(\mathbf{x}) + s\varepsilon^{\text{bg}}(\mathbf{x}) , \quad (28)$$

and $\hat{\zeta}$,

$$\hat{\zeta} = s\mu_0 . \quad (29)$$

The domain encloses an inaccessible volume action antenna source domain $\mathbb{D}^{\text{src}} \not\subset \mathbb{D}$ which contains the transmitting and receiving antennas. The only fields present are the electromagnetic background wavefields. In state B, we have the same spatial domain \mathbb{D} and the same medium parameters where in this case the boundary $\partial\mathbb{D}$ also encloses a domain \mathbb{D}^{sct} , due to the presence of an object with medium parameters $\hat{\eta}^{\text{sct}}(\mathbf{x})$ and $\hat{\zeta}$.

For these two states the reciprocity theorem is written as

$$\begin{aligned} \epsilon_{m,r,p} \int_{\mathbf{x} \in \partial\mathbb{D}} \nu_m \left[\hat{E}_r^A(\mathbf{x}) \hat{H}_p^B(\mathbf{x}) - \hat{E}_r^B(\mathbf{x}) \hat{H}_p^A(\mathbf{x}) \right] dA \\ - \epsilon_{m,r,p} \int_{\mathbf{x} \in \partial\mathbb{D}^{\text{src}}} \nu_m \left[\hat{E}_r^A(\mathbf{x}) \hat{H}_p^B(\mathbf{x}) - \hat{E}_r^B(\mathbf{x}) \hat{H}_p^A(\mathbf{x}) \right] dA \\ = \int_{\mathbf{x} \in \mathbb{D}} -[\eta_{r,k}^B(\mathbf{x}) - \eta_{k,r}^A(\mathbf{x})] \hat{E}_r^A(\mathbf{x}) \hat{E}_k^B(\mathbf{x}) dV . \quad (30) \end{aligned}$$

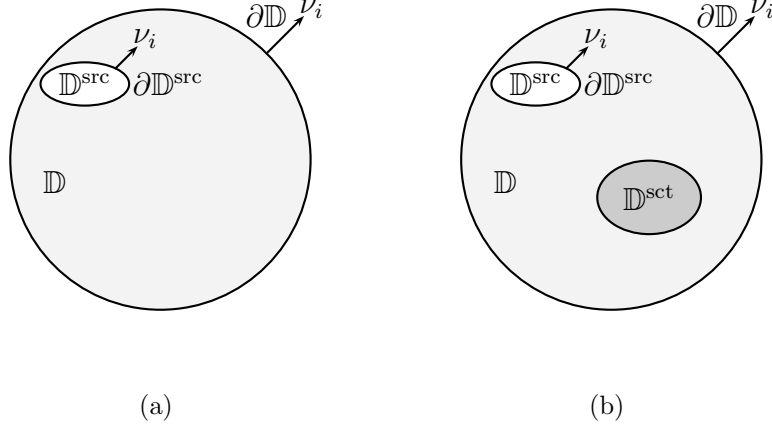


Figure 8: Two states of the same spatial domain \mathbb{D} with boundary $\partial\mathbb{D}$ and with inaccessible volume action antenna source domain $\mathbb{D}^{\text{src}} \not\subset \mathbb{D}$. The source domain contains a receiving and transmitting antenna. In state A (a) the electromagnetic properties are $\hat{\eta}^A(\mathbf{x}) = \hat{\eta}(\mathbf{x})$ and $\hat{\zeta}^A = \hat{\zeta}$, and state B (b) has the same background medium and a scattering domain $\mathbb{D}^{\text{sct}} \subset \mathbb{D}$, with $\hat{\eta}^B(\mathbf{x}) = \hat{\eta}^{\text{sct}}(\mathbf{x})$ and $\hat{\zeta}^B = \hat{\zeta}$.

The first integral over the outer boundary vanishes, since in both states the medium parameters outside $\partial\mathbb{D}$ are the same, and since there are no sources outside $\partial\mathbb{D}$. The boundary integral over the source domain can be approximated as follows by putting, in the low frequency range,

$$\hat{E}_i(\mathbf{x}) = -\partial_i \hat{\phi}(\mathbf{x}) , \quad (31)$$

where $\hat{\phi}$ is the electric potential. Using Stokes' theorem the integral over the boundary of the source domain is obtained as

$$\epsilon_{m,r,p} \int_{\mathbf{x} \in \partial\mathbb{D}^{\text{src}}} \nu_m \left[\hat{E}_r^A(\mathbf{x}) \hat{H}_p^B(\mathbf{x}) - \hat{E}_r^B(\mathbf{x}) \hat{H}_p^A(\mathbf{x}) \right] dA = \int_{\mathbf{x} \in \partial\mathbb{D}^{\text{src}}} \nu_m \left[\hat{\phi}^A(\mathbf{x}) \hat{\eta}^B(\mathbf{x}) \hat{E}_m^B(\mathbf{x}) - \hat{\phi}^B(\mathbf{x}) \hat{\eta}^A(\mathbf{x}) \hat{E}_m^A(\mathbf{x}) \right] dA . \quad (32)$$

The antennas in the source domain are described as perfect conductors which form a N-ports system, where each termination port has a surface \mathbb{A}_α , for $\alpha = 1, \dots, N$. Since the electric potential $\hat{\phi}^{A,B}(\mathbf{x})$ is constant over such a termination port, each terminal α has a constant potential \hat{V}_α . At each port the Maxwell current density $\hat{J}_k(\mathbf{x}) + s\hat{D}_k(\mathbf{x})$ is dominated by the electric current density $\hat{J}_k(\mathbf{x})$ in the low frequency approximation and consequently the electric line current density I_α is used. So from the constitutive relations in combination with the electromagnetic boundary conditions the right-hand

side of equation (32) is written as a finite summation over the terminals, i.e.,

$$\begin{aligned}
& \int_{\mathbf{x} \in \partial \mathbb{D}^{\text{src}}} \nu_m \left[\hat{\phi}^A(\mathbf{x}) \hat{\eta}^B(\mathbf{x}) \hat{E}_m^B(\mathbf{x}) - \hat{\phi}^B(\mathbf{x}) \hat{\eta}^A(\mathbf{x}) \hat{E}_m^A(\mathbf{x}) \right] dA \\
&= \sum_{\alpha=1}^N \int_{\mathbf{x} \in \mathbb{A}_\alpha} \nu_m \left[\hat{\phi}^A(\mathbf{x}) \hat{J}_m^B(\mathbf{x}) - \hat{\phi}^B(\mathbf{x}) \hat{J}_m^A(\mathbf{x}) \right] dA \\
&= \sum_{\alpha=1}^N \left[\hat{V}_\alpha^A \hat{I}_\alpha^B - \hat{V}_\alpha^B \hat{I}_\alpha^A \right] . \quad (33)
\end{aligned}$$

The electric potentials and line current densities in the antennas are coupled via the impedance matrix $\hat{Z}_{\alpha\beta}$ as

$$\hat{V}_\alpha = \hat{Z}_{\alpha\beta} \hat{I}_\beta \quad \text{for } \{\alpha, \beta\} = 1, \dots, N . \quad (34)$$

Combining equations (30), (32) and (33) with the state descriptions as formulated in table 1 results in

$$\delta \hat{Z}_{\alpha\beta} \hat{I}_\alpha^A \hat{I}_\beta^B = - \int_{\mathbf{x} \in \mathbb{D}} [\eta^B(\mathbf{x}) - \eta^A(\mathbf{x})] \hat{E}_k^A(\mathbf{x}) \hat{E}_k^B(\mathbf{x}) dV , \quad (35)$$

where $\delta \hat{Z}_{\alpha\beta}$ is the difference in impedance between two states,

$$\delta \hat{Z}_{\alpha\beta} = \hat{Z}_{\alpha\beta}^A - \hat{Z}_{\alpha\beta}^B . \quad (36)$$

The electric field strength is linearly dependent on the electric line current density $\hat{I}_\alpha^{A,B}$, so

$$\hat{E}_k^{A,B}(\mathbf{x}) = \hat{e}_{\alpha;k}^{A,B}(\mathbf{x}) \hat{I}_\alpha^{A,B} , \quad (37)$$

in which $\hat{e}_{\alpha;k}^A = \hat{e}_{\alpha;k}^{\text{bg}}$ and $\hat{e}_{\alpha;k}^B = \hat{e}_{\alpha;k}^{\text{tot}}$ are the electric field strengths caused by their unit current densities. Substitution of equation (37) in equation (35) gives an integral equation describing the change of impedance, $\delta \hat{Z}_{\alpha\beta}$, due to an anomaly $\delta \hat{\eta}(\mathbf{x}) = \hat{\eta}^{\text{bg}}(\mathbf{x}) - \hat{\eta}^{\text{set}}(\mathbf{x})$ in the background medium, viz.,

$$\delta \hat{Z}_{\alpha\beta} = \int_{\mathbf{x} \in \mathbb{D}} \delta \hat{\eta}(\mathbf{x}) \hat{e}_{\alpha;k}^{\text{bg}}(\mathbf{x}) \hat{e}_{\beta;k}^{\text{tot}}(\mathbf{x}) dV . \quad (38)$$

This integral equation will serve as a starting point for the imaging algorithm.

3.2 Measuring in bistatic mode

Based on the design presented in section 2 of this chapter a bistatic antenna system has been built. Applying equation (34) to this setup, ($N = 2$), we obtain the following equation

$$\hat{V}_2 = \hat{Z}_{21} \hat{I}_1 + \hat{Z}_{22} \hat{I}_2 , \quad (39)$$

where \hat{V}_2 represents the voltage measured at the receiver, \hat{I}_1 the electric source current at the transmitter, \hat{Z}_{21} the mutual impedance of the transmitter and the receiver and \hat{Z}_{22}

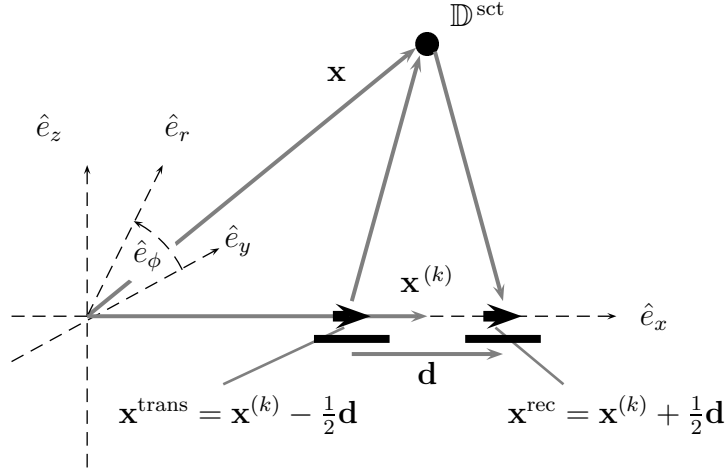


Figure 9: The setup in bistatic mode.

the self impedance of the receiver. Note that we assume the medium to be reciprocal and consequently $\hat{Z}_{12} = \hat{Z}_{21}$. Since the receiver voltage is measured over an open end port, the current through the receiver equals zero, $\hat{I}_2 = 0$. Therefore the measured voltage at the receiver, \hat{V}_2 , in equation (39) equals

$$\hat{V}^{\text{rec}} = \hat{Z}_{12} \hat{I}^{\text{trans}} , \quad (40)$$

since $\hat{V}_2 = \hat{V}^{\text{rec}}$ and $\hat{I}_1 = \hat{I}^{\text{trans}}$.

In figure 9 it is shown how in a bistatic setup measurements take place at ‘discrete’ positions $\mathbf{v}^{(k)}$ for the system, viz.

$$\mathbf{v}^{(k)} = (x^{(k)}, 0, \phi^{(k)}) . \quad (41)$$

Adapting integral equation (38) for these discrete positions and combining it with the results shown in equation (40), we obtain the following integral equation

$$\frac{\delta \hat{V}^{\text{rec}}(\mathbf{v}^{(k)})}{\hat{I}^{\text{trans}}} = \int_{\mathbf{v} \in \mathbb{D}} \delta \eta(\mathbf{v}) \hat{S}(\mathbf{v} | \mathbf{v}^{(k)}) dV , \quad (42)$$

in which the sensitivity function $\hat{S}(\mathbf{v} | \mathbf{v}^{(k)})$ describes the combination of the transmitter and receiver patterns of the antenna system,

$$\begin{aligned} \hat{S}(\mathbf{v} | \mathbf{v}^{(k)}) &= \hat{S}(x - x^{(k)}, r, \phi - \phi^{(k)}) \\ &= \hat{e}_j^{\text{trans;bg}}(x - x^{(k)} + \frac{1}{2}d, r, \phi - \phi^{(k)}) \hat{e}_j^{\text{rec;bg}}(x - x^{(k)} - \frac{1}{2}d, r, \phi - \phi^{(k)}) , \end{aligned} \quad (43)$$

where $\hat{e}_j^{\text{trans;bg}}(\mathbf{v})$ and $\hat{e}_j^{\text{rec;bg}}(\mathbf{v})$ are the electric wavefields in the background medium produced by an electric unit current at the transmitter and the receiver position, respectively. These radiation patterns are approximately equal to the patterns computed at the central frequency of 100 MHz. Note that the Born approximation is used to approximate $\hat{e}_j^{\text{rec;tot}}(\mathbf{v})$ by $\hat{e}_j^{\text{rec;bg}}(\mathbf{v})$. Besides, we assume the contrast to be frequency independent, $\delta \hat{\eta}(\mathbf{v}) = \delta \eta(\mathbf{v})$.

In view of the presence of convolution and periodicity in the angular direction, we take advantage of the properties of discrete Fourier series. This series is defined as

$$f(\phi) = \sum_{n=-\infty}^{\infty} f^{(n)} e^{in\phi} , \quad (44)$$

where

$$f^{(n)} = \frac{1}{2\pi} \int_{\phi=0}^{2\pi} f(\phi) e^{-in\phi} d\phi . \quad (45)$$

Applying these discrete Fourier transforms to equation (42) leads to decoupled equations in the discrete angular Fourier domain

$$\frac{\delta \hat{V}^{(n);\text{rec}}(x^{(k)})}{\hat{I}^{\text{trans}}} = \int_{x=-\infty}^{\infty} \int_{r=0}^{\infty} \delta \eta^{(n)}(x, r) \hat{S}^{(n)}(x - x^{(k)}, r) r dr dx \quad \forall \quad n = -\infty, \dots, \infty , \quad (46)$$

where

$$\hat{S}^{(n)}(x, r) = \frac{1}{2\pi} \int_{\phi=0}^{2\pi} e^{-in\phi} \hat{S}(x, r, \phi) d\phi , \quad (47)$$

$$\delta \hat{V}^{(n);\text{rec}}(x^{(k)}) = \frac{1}{2\pi} \int_{\phi=0}^{2\pi} e^{-in\phi} \delta \hat{V}^{\text{rec}}(x^{(k)}, \phi) d\phi , \quad (48)$$

and

$$\delta \eta^{(n)}(x, r) = \frac{1}{2\pi} \int_{\phi=0}^{2\pi} e^{-in\phi} \delta \eta(x, r, \phi) d\phi . \quad (49)$$

Replacing the latter integrals by finite summations using a trapezoidal integration rule, we arrive at

$$\hat{S}^{(n)}(x, r) = \frac{1}{2\pi} \sum_{m=1}^M e^{-inm\Delta\phi^{(k)}} \hat{S}(x, r, m\Delta\phi^{(k)}) \Delta\phi^{(k)} , \quad (50)$$

$$\delta \hat{V}^{(n);\text{rec}}(x^{(k)}) = \frac{1}{2\pi} \sum_{m=1}^M e^{-inm\Delta\phi^{(k)}} \delta \hat{V}^{\text{rec}}(x^{(k)}, m\Delta\phi^{(k)}) \Delta\phi^{(k)} \quad (51)$$

and

$$\delta \eta^{(n)}(x, r) = \frac{1}{2\pi} \sum_{m=1}^M e^{-inm\Delta\phi^{(k)}} \delta \eta(x, r, m\Delta\phi^{(k)}) \Delta\phi^{(k)} , \quad (52)$$

where $M\Delta\phi^{(k)} = 2\pi$. After an estimate in the angular Fourier domain for $\delta \eta^{(n)}(x, r)$ for $-N \leq n \leq N$ is obtained, an image of the contrast $\delta \eta(x, r, \phi)$ in the spatial domain is derived from

$$\delta \eta(x, r, \phi) = \sum_{n=-N}^N \delta \eta^{(n)}(x, r) e^{in\phi} . \quad (53)$$

3.3 Imaging in bistatic mode

In order to obtain an estimate for $\delta\eta^{(n)}(\mathbf{v})$ we define the following error functional $F^{(n)}$,

$$F^{(n)} = \sum_{x^{(k)}} \sum_{\omega} \left| \frac{\delta\hat{V}^{(n);\text{rec}}(x^{(k)}, \omega)}{\hat{I}^{\text{trans}}} - \int_{x=-\infty}^{\infty} \int_{r=0}^{\infty} \delta\eta^{(n)}(x, r) \hat{S}^{(n)}((x, r)|(x^{(k)}, r), \omega) r dr dx \right|^2 \Delta x^{(k)} \Delta \omega . \quad (54)$$

Using the following notation in the functional $F^{(n)}$ for $\delta\eta^{(n)}(x, r)$

$$\delta\eta^{(n)}(x, r) = \alpha^{(n)} \Delta\eta^{(n)}(x, r) , \quad (55)$$

where $\alpha^{(n)}$ is a real constant and $\Delta\eta^{(n)}(x, r)$ is an update direction, this functional tends to its minimum when $\alpha^{(n)}$ satisfies

$$\alpha^{(n)} = \frac{\Re \left\{ \sum_{x^{(k)}} \sum_{\omega} \frac{\delta\hat{V}^{(n);\text{rec}}(x^{(k)}, \omega)}{\hat{I}^{\text{trans}}} \left[\int_{x=-\infty}^{\infty} \int_{r=0}^{\infty} \Delta\eta^{(n)}(x, r) \hat{S}^{(n)}((x, r)|(x^{(k)}, r), \omega) r dr dx \right]^* \right\}}{\sum_{x^{(k)}} \sum_{\omega} \left| \int_{x=-\infty}^{\infty} \int_{r=0}^{\infty} \Delta\eta^{(n)}(x, r) \hat{S}^{(n)}((x, r)|(x^{(k)}, r), \omega) r dr dx \right|^2} . \quad (56)$$

We interchange the summations and the integrations in the numerator in the right-hand side of this equation. Then we observe that, apart from a constant, this numerator is maximized by taking the update direction to be

$$\Delta\eta^{(n)}(x, r) = \sum_{x^{(k)}} \sum_{\omega} \left(\hat{S}^{(n)}(x - x^{(k)}, r, \omega) \right)^* \frac{\delta\hat{V}^{(n);\text{rec}}(x^{(k)}, \omega)}{\hat{I}^{\text{trans}}} . \quad (57)$$

Substituting this direction in the numerator of the right-hand side of equation (56) we observe that the constant $\alpha^{(n)}$ equals

$$\alpha^{(n)} = \frac{\int_{x=-\infty}^{\infty} \int_{r=0}^{\infty} |\Delta\eta^{(n)}(x, r)|^2 r dr dx}{\sum_{x^{(k)}} \sum_{\omega} \left| \int_{x=-\infty}^{\infty} \int_{r=0}^{\infty} \Delta\eta^{(n)}(x, r) \hat{S}^{(n)}(x - x^{(k)}, r, \omega) r dr dx \right|^2} . \quad (58)$$

Note that $\alpha^{(n)}$ is indeed real and independent of the parameters x , r and ω . Furthermore it is noted that the update direction of equation (57) represents the back propagation of the data from the data domain to the domain of observation. A summation of the update directions over all angular contributions leads to a first image of the contrast $\delta\eta(\mathbf{v})$ in the subsurface, viz.

$$\delta\eta(\mathbf{v}) = \sum_{n=-N}^N \Delta\eta^{(n)}(x, r) . \quad (59)$$

An improved image is obtained when we take into account the minimization constant $\alpha^{(n)}$. In that case $\delta\eta(\mathbf{v})$ is obtained via

$$\delta\eta(\mathbf{v}) = \sum_{n=-N}^N \alpha^{(n)} \Delta\eta^{(n)}(x, r) . \quad (60)$$

Note that this minimization procedure is in fact the initial iteration of a conjugate gradient inversion method. By applying such a scheme, further improvements may be achieved, as shown previously for a synthetic example [4]. In the next subsection we present some results based on the two imaging procedures of equations (59) and (60). The former procedure is denoted as the back propagation algorithm, while the latter is denoted as the minimized back propagation algorithm.

3.4 Imaging Results

Both the back propagation and the minimized back propagation algorithms are tested on synthetic and measured data. In both cases ‘measurements’ take place at 64 angular positions.

First we consider a synthetic case, where the homogeneous background medium is characterized by the parameters $\sigma = 0$ and $\varepsilon_r = 80$. At a radial distance of two meter in the plane $x = 0$ a point scatterer is positioned with medium parameters $\varepsilon_r = 160$ and $\sigma = 1$ S/m. Synthetic data are obtained using equation (42). Results from both image processing procedures are given in figures 10(a) and 10(b). In these figures the computed contrast $\delta\eta(\mathbf{v})$ is shown in the plane $x = 0$. Comparing the results of the two procedures, we observe the expected increase in resolution in the angular direction.

Secondly, we consider a field data set where the data are obtained with the antenna system positioned in a swimming pool. As scattering object, a metallic gas bottle is positioned in front of the system at a radial distance of two meters. Since the source wavelet and thus the frequency spectrum of the electric current density at the transmitter is unknown, we simply take \hat{I}^{trans} to be equal to one in the image procedure. The measured voltage, contains the signals due to reception of both the direct and the scattered electromagnetic waves. These data are corrected for the direct wave, by subtracting the first trace, $\phi = 0$, from the data set of each trace. The corrected data, shown in figure 11, are used as input data for both the back propagation and the minimized back propagation algorithm. The image results are shown in figures 12(a) and 12(b). The figures show the computed contrast for the plane $x = 0$.

Comparing the results of the synthetic and the measured example we observe a similar behaviour of the angular dependence of the image distributions.

There are great similarities between the images based on synthetic and measured data, especially in the angular direction. The blurring effect in the radial direction in the image from the measured data is caused through antenna ringing. This effect should be but isn’t taken into account in the transmitter current where as source wavelet an impulse function in time is taken. Therefore a deconvolution for the wavelet is omitted and consequently the algorithm will ‘interpret’ the long ringing wavelet as being caused by several reflections from a couple of objects behind each other.

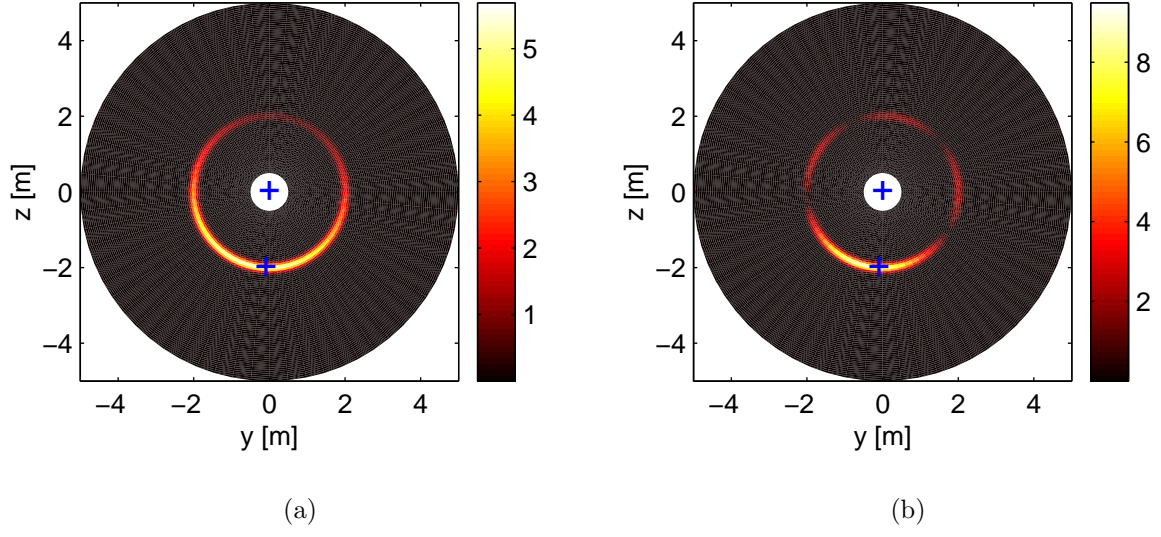


Figure 10: The computed contrast obtained from synthetic data, via (a) back propagation: $\delta\eta^{(n)}(x, r) = \Delta\eta^{(n)}(x, r)$ and (b) minimized back propagation: $\delta\eta^{(n)}(x, r) = \alpha^{(n)}\Delta\eta^{(n)}(x, r)$. The crosses denote the position of the antenna system in the center and the object at a radial distance of two meters.

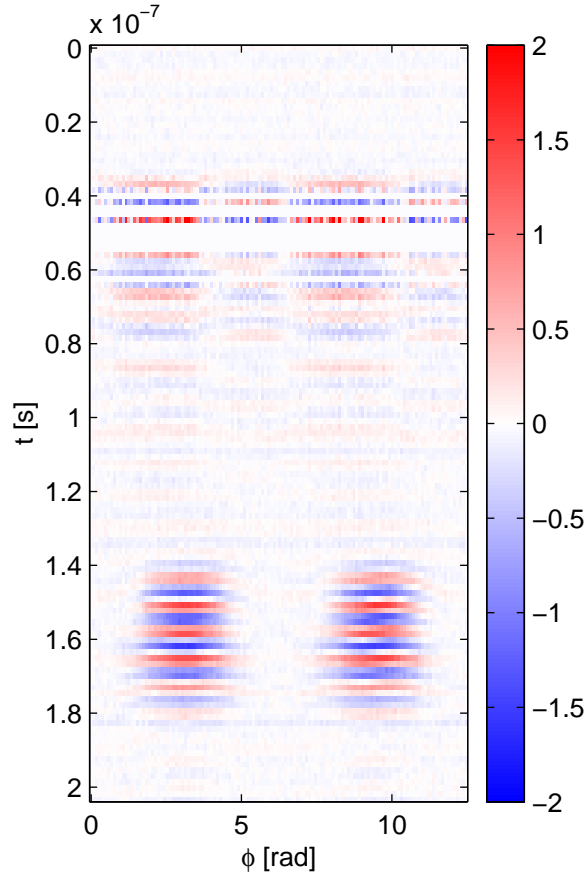


Figure 11: The measured receiver voltage as a function of time and angular position.

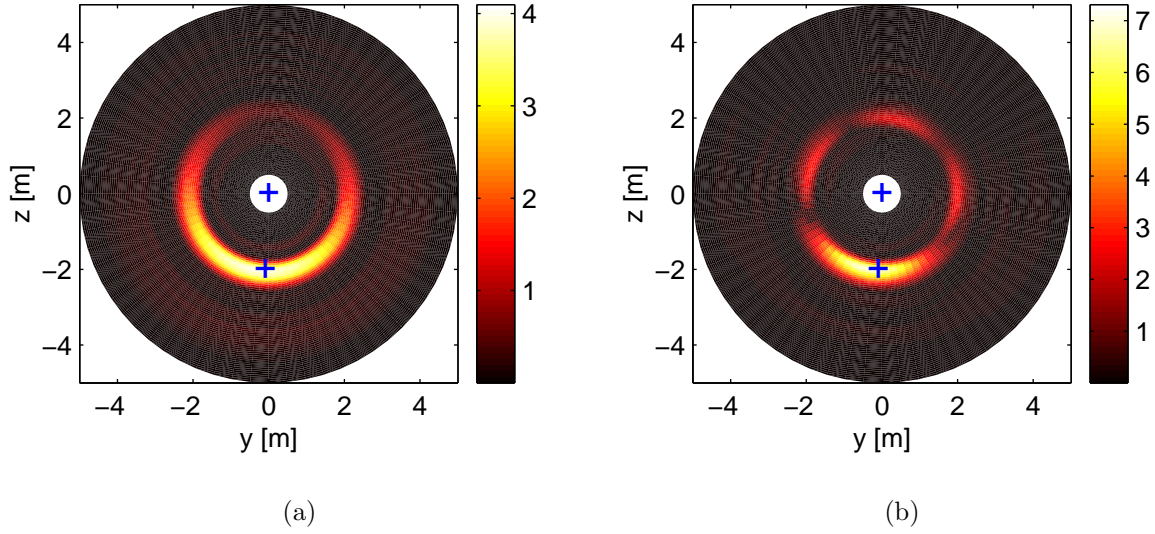


Figure 12: The computed contrast for measured data based on (a) back propagation: $\delta\eta^{(n)}(x, r) = \Delta\eta^{(n)}(x, r)$ and (b) minimized back propagation: $\delta\eta^{(n)}(x, r) = \alpha^{(n)}\Delta\eta^{(n)}(x, r)$. The crosses denote the position of the antenna system in the center and the object at a radial distance of two meters.

4 Conclusions

In this chapter we have discussed the antenna design of a directional borehole radar system. The modeling of the shielded antenna of this radar system was formulated as an integral equation for the unknown electric surface current density at the surface of the perfectly conducting reflector. This integral equation was numerically solved using an iterative conjugate gradient method; its efficiency was enhanced using a FFT routine for the computation of the convolution in the antenna direction. Based on the modeling results a prototype antenna system was built. The measured radiation pattern was compared with the computed one and they were in close agreement. Furthermore, a simple imaging algorithm based on back propagation has been proposed. Using the computed radiation pattern in this imaging procedure, a deconvolution of the radiation pattern in the angular direction was carried out. Finally we have improved this image procedure by carrying out a minimization procedure where the back propagation is used as an update direction. The result is an increase in angular resolution. We expect improved resolution in radial direction when we take the correct source wavelet. In practice a proper estimate of this source wavelet is difficult to obtain.

Acknowledgement

The prototype of the antenna system has been built in cooperation with T&A Radar, Netherlands Organization for Applied Scientific Research (TNO-FEL) and National Aerospace Laboratory (NLR) and partly supported by CODEMA, a committee of the Dutch Ministry of Defense. In particular the authors would like to acknowledge the support of

Robert van Ingen and Michiel van Oers, T&A RADAR, and Jelle Rodenhuis, TNO-FEL.

References

- [1] Zwamborn A.P.M. and van den Berg P.M., “*A weak form of the conjugate gradient FFT method for plate problem*”, IEEE Transactions on Antennas and Propagation, 1991, vol. 39, pp. 224-228
- [2] Abramowitz M. and Stegun I.A., “*Handbook of mathematical functions*”, Dover Publications, New York, 1970.
- [3] de Hoop A.T., “*Handbook of Radiation and Scattering of Waves*”, Academic Press, London, 1995, chapter 28.
- [4] van Dongen K.W.A., van den Berg P.M. and Fokkema J.T., “*A directional borehole radar: numerical and experimental verification*”, 2001 IEEE AP-S International Symposium and USNC/URSI National Radio Science Meeting, Boston, USA, 8-13 July 2001, Vol. II, ISBN 0 7803 7070 8, pp. 746-749.